Non-classical crystallization pathway of transition metal phosphate compounds

Stephanos Karafiludis[1,2*], Zdravko Kochovski[3], Ernesto Scoppola[4], Anika Retzmann[1], Vasile-Dan Hodoroaba[1], Johan E. ten Elshof[5], Franziska Emmerling[1,2], and Tomasz M. Stawski[1**]

[1]Federal Institute for Materials Research and Testing, Richard-Willstatter-Straße 11, 12489 Berlin, Germany
[2]Department of Chemistry, Humboldt-Universität zu Berlin, Brook-Taylor-Straße 2, 12489 Berlin
[3]Department for Electrochemical Energy Storage, Helmholtz-Zentrum Berlin for Materials and Energy, Hahn-Meitner Platz 1, 14109 Berlin, Germany
[4]Biomaterials, Hierarchical Structure of Biological and Bio-inspired Materials, Max Planck Institute of Colloids and Interfaces, Potsdam 14476, Germany.
[5]MESA+ Institute for Nanotechnology, University of Twente, P.O. Box 217, 7500 AE Enschede, the Netherlands

Stephanos Karafiludis: https://orcid.org/0000-0002-7257-6311 ;
Zdravko Kochovski: https://orcid.org/0000-0001-8375-0365 ;
Ernesto Scoppola: https://orcid.org/0000-0002-6390-052X ;
Anika Retzmann: https://orcid.org/0000-0002-0208-5453 ;;
Vasile-Dan Hodoroaba: https://orcid.org/0000-0002-7901-6114 ;
Johan E. Ten Elshof: https://orcid.org/0000-0001-7995-6571 ;
Franziska Emmerling: https://orcid.org/0000-0001-8528-0301 ;
Tomasz M. Stawski: https://orcid.org/0000-0002-0881-5808 ;

Corresponding authors: **tomasz.stawski@bam.de ;* stephanos.karafiludis@bam.de

Keywords: nucleation, multi-step process, intermediate phases, transition metals, phosphates, liquid-liquid phase separation, amorphous phases

Abstract

Here, we elucidate non-classical multistep crystallization pathways of transition metal phosphates from aqueous solutions. We followed precipitation processes of M-struvites, $NH_4MPO_4 \cdot 6H_2O$, and M-phosphate octahydrates, $M_3(PO_4)_2 \cdot 8H_2O$, where M = Ni, Co, Ni_xCo_{1-x} by using *in-situ* scattering and spectroscopy-based techniques, supported by elemental mass spectrometry analyses and advanced electron microscopy. Ni- and Co-phosphates crystallize via intermediate colloidal amorphous nanophases which subsequently change their complex structures while agglomerating, condensing, and densifying throughout the extended reaction times. We reconstructed the three-dimensional morphology of these precursors by employing cryo-electron tomography (cryo-ET). We found that the complex interplay between metastable amorphous colloids and proto-crystalline units determines the reaction pathways. Ultimately, the same crystalline structure, such as struvite, is formed. However, the multistep process stages vary in complexity and can last from a few minutes to several hours depending on the selected transition metal(s), their concentration, and the Ni:Co ratio.

Introduction

A key factor in ensuring the sustainable use of raw materials to meet global demand has been the recovery and reuse of key components. Phosphate, PO_4^{3-} and many transition metals are listed as critical raw materials[1-3]. Moreover, these elements may cause adverse effects in the environment. Phosphorous is the major culprit in anthropogenic eutrophication. Transition metal ions are toxic pollutants, especially in ground- and wastewater. Therefore, co-precipitation of phosphate and transition metal-bearing phases from various waste streams of agricultural, industrial, or mining origin (tailings, sludge, wastewaters etc.) is a viable extraction and recycling method to yield transition metal phosphates (TMPs) [4, 5]. Such materials could be further upcycled into processed, higher value compounds suitable for applicational use. For example, transition metal phosphates such as Zr-[6], Sn-[7], Ni- or Co-[8] phosphates garnered attention as low-cost, chemically stable and tunable proton conductors for fuel cells [9-16]. However, to effectively harvest metal and phosphate in a form of TMPs and convert them to functional materials, one needs to elucidate their nucleation and crystallization pathways from aqueous solutions. Although, the synthesis and precipitation of Mg or Ca phosphate-bearing phases are relatively well characterized [17-19], investigations of the crystallization of transition metal phosphate materials are relatively scarce and focus on mineralogical aspects[20]. Most of the available studies concentrate on the incorporation or adsorption of transition metals and metalloids[10, 21-24] rather than their complete substitution in phosphate-based compounds [25-27]. However, TMPs exhibit in their crystallization pathways, growth kinetics, thermodynamic stabilities, or transformations major differences among each other and differ from their related main-group analogues [28, 29].

The traditional view of crystallization and nucleation through a classical model has been widely used to describe chemical systems since its establishment in the 19th century [30, 31]. This is mainly because of its simplicity and ability to make accurate predictions. The classical crystallization theory (CCT) assumes a layer-by-layer growth of primary crystal nuclei due to the adsorption of growth units/ monomers (atoms, ions, molecules etc.) on the crystal surface/kinks and their following reconfiguration to a new interface. Although CCT works well for model systems [32, 33], a frequent number of complex interactions could not be explained by this theory due to its simplified assumptions and limitations *i.e.* capillary assumption or considering only single particle attachment. Theoretical predictions tend to deviate significantly from experimental results in orders of magnitudes in nucleation and reaction rates of the crystalline particles [34-38]. Different experimental studies and approaches demonstrated empirically multiple possible formation pathways toward the final crystal through the inclusion of prenucleation clusters [39], liquid droplets, gels, primary amorphous or crystalline nanoparticles, nanoaggregates[4] or mesocrystals[40]. In the past two decades, a large variety of these transitional precursor phases of crystalline substances were discovered in pharmaceuticals [41, 42], proteins [43-45], organic molecules [46, 47], thin films [48, 49], biominerals [39, 50] and inorganic materials [4, 46, 51-53].

As we demonstrate in this work, TMPs follow a non-classical crystallization pathway, which includes evolving amorphous precursors prior to the final formation of a crystal. We holistically elucidate the crystallization behavior of transition metal phosphate phases, from

their intermediate amorphous nanophases in solution, through aggregates, proto-crystalline units, to final crystals. The formation processes are in-detail analyzed with various diffraction- and spectroscopy-based ex- and *in-situ* approaches. Ni and Co ions can be both incorporated into the same crystalline structures (*i.e.* struvite or octahydrate). However, the crystallization stages of these analogous TMPs are essentially different [4, 54]. We also demonstrate that in a dual Ni_xCo_{1-x} metal mixture compared to the pure cases, even more complex pathway is induced. Here, the Ni:Co ratio and the concentration of both metals have a major influence on the reaction kinetics and the crystallization outcome. In this work, we provide insights into how two 3d metal ions, Ni and Co, interact with each other resulting in changes in reaction time and crystallization stages of the phosphate precipitation.

Methods

Synthesis

$(NH_4)_2HPO_4$ (DAP) (ChemSolute, 99%), $NiSO_4{\cdot}6H_2O$ (ChemSolute, 99%) and $CoSO_4{\cdot}7H_2O$ (Alfa Aesar, 98%) were used to synthesize M-phosphates (M = Ni, Co, Ni_xCo_{1-x}). At first, 1 mol/l stock solutions of DAP and the metal salts were prepared. The detailed synthesis procedure can be found elsewhere[4]. The transition metal and DAP concentrations in the aqueous solution were varied from 0.004 mol/l to 1 mol/l resulting in a metal-to-phosphate ratio between $0.2 \leq MP \leq 1$. By using DAP with a fixed nitrogen-to-phosphate ratio of 2 the occurring precipitation reaction of M-struvite was typically occurring according to the following mass-balance equation:

$$6H_2O + NH_4^+{}_{(aq)} + H_xPO_4^{3-x}{}_{(aq)} + M^{2+}{}_{(aq)} \rightarrow NH_4MPO_4 \cdot 6H_2O_{(s)} + xH^+{}_{(aq)} \quad (1)$$

Equation (1) was in general valid for Ni regardless of the metal concentration used, as well as for Co at lower concentrations below a MP ratio of 0.4 [54]. However, at high concentrations of $Co^{2+,}$ above a MP ratio of 0.4 we observed the crystallization of cobalt(II)phosphate octahydrate (CPO) instead of Co-struvite (COS) according to eq. (2):

$$8H_2O + 2\ H_xPO_4^{3-x}{}_{(aq)} + 3\ Co^{2+}{}_{(aq)} \rightarrow Co_3(PO_4)_2 \cdot 8H_2O_{(s)} + 2xH^+{}_{(aq)} \quad (2)$$

We also investigated (Ni_xCo_{1-x})-mixtures, for which we defined Ni numbers (Ni#). Following eq. (3), we varied Ni# from 0.1 (Co-rich) to 0.95 (Ni-rich).

$$Ni\# = \frac{c(Ni^{2+})}{c(Ni^{2+}) + c(Co^{2+})} \quad (3)$$

For any analyses requiring dry crystalline powders, the solid phases precipitated in solutions were collected onto a cellulose filter (pore size 1 µm, LABSOLUTE) by using a vacuum filtration kit (*i.e.* Büchner funnel). Afterwards, the powders were washed with distilled water and left to dry at room temperature in air for 2 hours.

To elucidate the crystal formation pathways, we used various *in-situ* and *ex-situ* characterization methods (Table 1), with which we analyzed solids in solution, dry solids, and supernatants, etc. at different stages. Detailed technical descriptions of the used characterization methods, including X-ray diffraction (XRD) for identification of the phase composition, pH measurements to monitor the precipitation reaction, infrared spectroscopy (IR) for tracking the phosphate and water/ammonium environment in the solids, scanning

electron microscopy (SEM), conventional- and cryogenic transmission electron microscopy (-CTEM, cryo-TEM) for imaging, diffraction and elemental mappings/line scans, *in-situ* small- and wide-angle X-ray scattering (SAXS/WAXS) for tracking amorphous phaser associated with the phase composition, and inductively coupled plasma mass spectrometry (ICP-MS) analysis for determining the changing chemical composition of liquid and solid as a function of time can be found in the ESI (ESI: *Methods*). The rationale behind the use of each method is described in Table 1.

Table 1: Summary of used methods and the associated research goal according to their importance. The crystallization process was analyzed by a combination of imaging, spectroscopic, spectrometric, and scattering based *ex-* and *in-situ* methods.

method	description	*ex-/in-situ*	solute/ solid/ both	research goal
SAXS/WAXS	Time-resolved X-ray scattering	*in-situ*	both	Time-resolved particle sizes of hierarchical structures, reaction kinetics, and mechanism
cryo-TEM	imaging and 3D reconstruction	*ex-situ*	solid	imaging morphology, size, and structure of amorphous phases
	diffraction	*ex-situ*	solid	determination of crystal structure
ICP-MS	dissolved solids	*ex-situ*	solid	elemental information about the solids
	particle filtered mother solution	*ex-situ*	solute	elemental information about the solutes
SEM	imaging	*ex-situ*	solid	imaging morphology, size, and structure of final crystalline phases
EDX	mapping & line scans	*ex-situ*	solid	elemental information about the solids
XRD	Powder, Bragg-Brentano	*ex-situ*	solid	phase composition
pH	time-resolved pH measurements	*in-situ*	both	reaction kinetics and mechanism
-CTEM	imaging	*ex-situ*	solid	imaging morphology, size, and structure of amorphous phases
EDX	mapping	*ex-situ*	solid	elemental information about the solids
FT-IR	attenuation	*ex-situ*	solid	elemental information & phase composition about the solids

Results and Discussion

Overview of the transitional nanophases during crystallization

The complexity of the crystallization pathways leading to a crystalline solid manifest themselves through changes in the solid material as well as in the complementary supernatant. Both pieces of this complementary "pair" need to be considered to fully understand the crystallization process. At the beginning of our investigations, we directly followed the reaction with usual laboratory methods including XRD or pH . We used all those observations to establish a baseline for advanced *in-situ* methods and pinpoint characteristic moments for *ex-situ* methods (Table 1). During the crystallization of TMPs protons are released (Eqs. 1 & 2), therefore, time-resolved pH measurements provide partial insights into the formation process of these materials. Thus, from simple pH trends, we can identify the characteristic events in the crystallization pathway and indeed confirm the multi-step nature of the mechanism. We further prove with various *in-situ* and *ex-situ* methods (Table 1) that the multi-step evolution involves transitional amorphous nanophases preceding the formation of the final crystals.

Moreover, a directly observable color change of the aqueous solutions/slurries of TMPs also hints towards potential phase evolution and indicates the multi-step character (*e.g.* transformations liquid-amorphous, liquid-amorphous, amorphous-crystalline). As we demonstrated in a previous work, the color change directly indicates an extensive change in the transition metal coordination environment associated with the transformation of the solids, *e.g.* from an amorphous to a crystalline state This involves further a structural ordering and reorganization [4]. Even by observing the evolving solutions, one can determine characteristic moments of time where the nature of solids changes, pointing out to a non-classical nature of the crystallization processes.

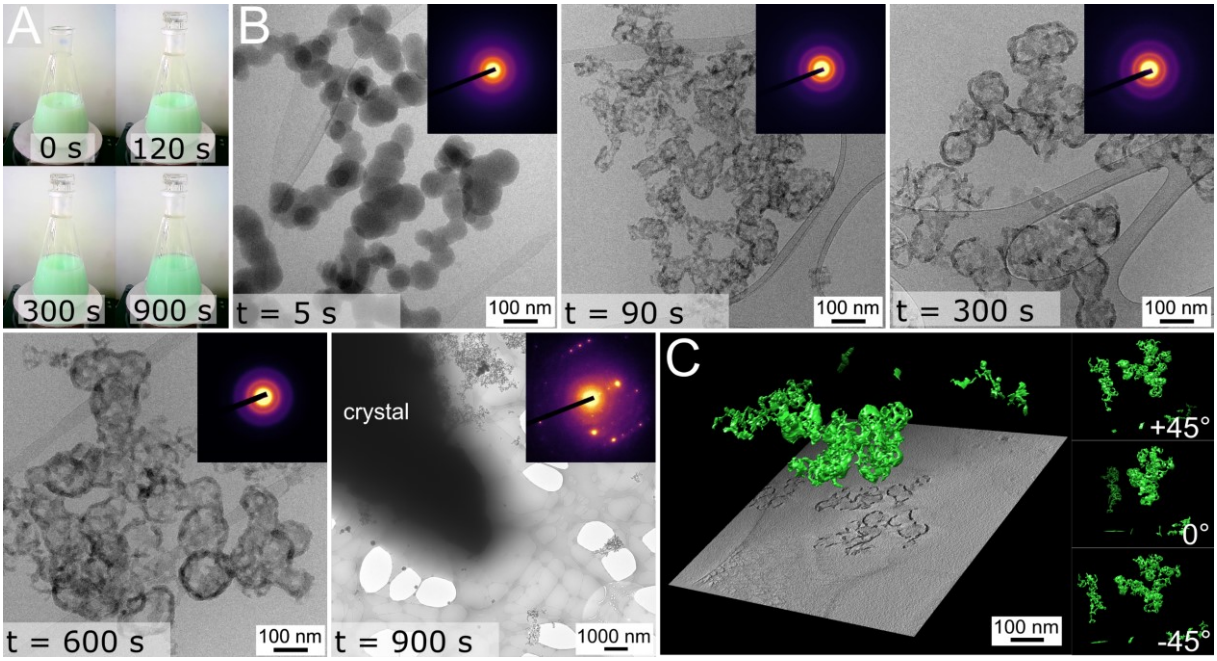

Figure 1: Cryo-TEM images and the tomographic reconstruction of Ni-phosphates at different reaction steps/times (*t* = 5 s, 90 s, 300 s, 600 s, and 900 s) in the precipitation reaction; (A) photographs of the temporal color changes in solution; (B) detailed cryo-TEM image of the observed structures at a given reaction time, inset:

associated SAED pattern; (C) three dimensional volume rendering from a cryo-ET reconstruction shown over a central XY slice from the reconstruction at *t* = 300 s, insets in C: The three-dimensional particle surface renderings in selected angles from -45° < 0° < +45° ; a full movie of the reconstruction and additional images can be found in the ESI: Figure S3. The measurements were supplemented with EDX maps in CTEM, with which we confirmed the presence of N, P, O, and M with M = Ni or Co in the observed aggregates but we also observed their decomposition by degassing of volatile compounds (ESI: Figure S3).

Accordingly, as indicated by the found pH trends (ESI: Figure S2) and the color changes, for investigations of the intermediate amorphous nanophases, cryo-TEM measurements were performed at selected reaction times for the pure Ni-system (Figure 1) and the pure Co-system (Figure 2). Importantly, Ni and Co exhibit clearly different reaction kinetics, where Ni fully develops within several minutes, while Co evolves over tens of minutes (≈10x factor difference). By the observation of the color change (Figure 1A and Figure 2A) and the pH trends (ESI: Figure S2), moments of interest in the crystallization pathway were selected and quenched using the cryo-TEM approach. Ideally, the interesting stages should comprise the formation of the smallest to the largest nucleating entities until their final transformation to a crystal.

Indeed, we observed complex amorphous particulate morphologies before any crystals were formed. For both Ni-PO_4 (Figure 1B) and Co-PO_4 (Figure 2B), the as-observed intermediate solids are amorphous as indicated by SAED (see the insets in each micrograph). Interestingly, the precursors have a three-dimensional (3D) morphology evidenced by the electron density contrast and branched agglomeration topology. Thus, even after the immediate pH drop due to mixing phosphate and metal solutions (ESI: Figure S2) associated with color change (Figure 1B), the initial moments of crystallization do not yield crystalline but amorphous solids. We visualized these 3D structural features in the complex amorphous framework of the nanophases by performing cryo-electron tomography (cryo-ET)[55]. In Figure 1C and**Fehler! Verweisquelle konnte nicht gefunden werden.**C a gallery of XY slices of the amorphous Ni- and Co-phosphate nanophases at *t* = 5 min (Ni) and *t* = 10 min (Co) are presented. Using segmentation and subsequent surface rendering of the particles in the tomographic reconstruction, the three-dimensional internal structure of the compounds can be revealed. At the early stages (*t* = 5 s) of the reaction, the Ni-system forms regular spherical amorphous nanoparticles of around 50 nm diameter agglomerated to µm-large frameworks (Figure 1B, C). With progressive reaction times (*t* = 90 s, 300 s and 900 s), the extent of agglomeration increases while particles also develop dense outer shells and hollow interiors (Figure 1C). From cryo-ET imaging, the observed structure comprises interconnected tubes with dense shells and voluminous interior. After *t* = 300 s, the agglomerates coalesce to a final µm-sized crystal of Ni-struvite at *t* = 900 s. These single crystals show a regular faceted morphology and exhibit usual diffraction spots in the SAED pattern. The actual transformation of the amorphous Ni-phases to a final crystal can be also correlated with the pH trends, where the pH equilibrates within five minutes regardless of the nickel concentration (ESI: Figure S2A-D).

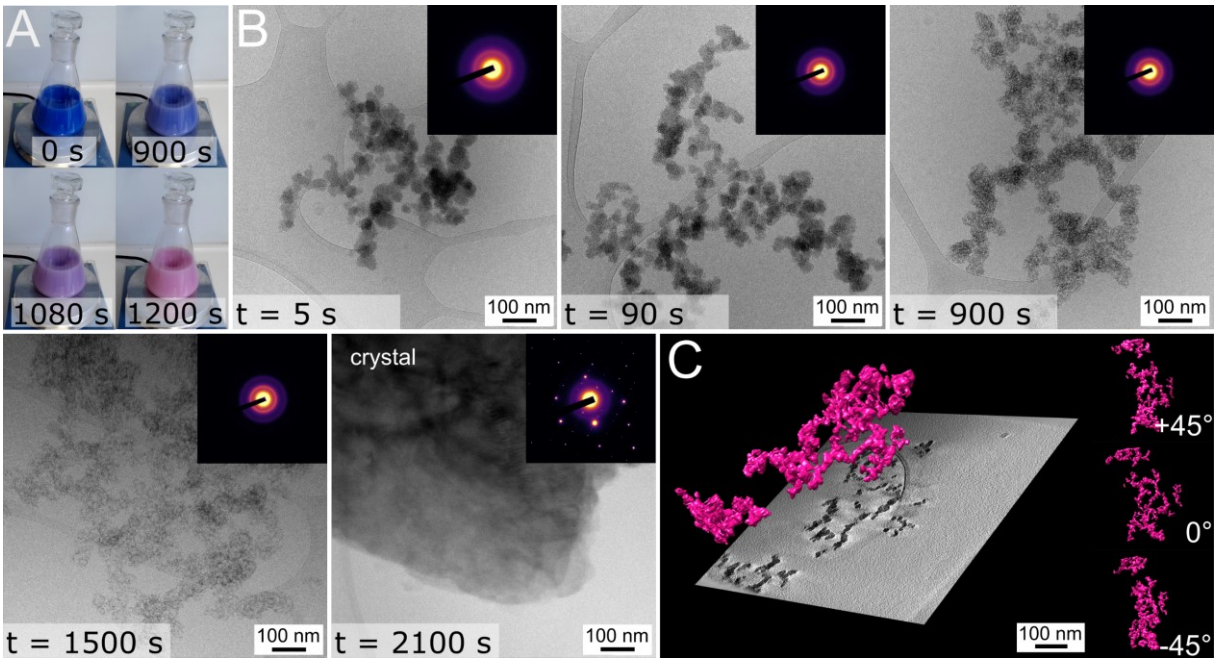

Figure 2: Cryo-TEM images and tomographic reconstruction of Co- phosphates at different reaction steps/times (*t* = 5 s, 90 s, 900 s, 1500 s, and 2100 s) in the precipitation reaction; (A) photographs of temporal color changes in solution; (B) detailed cryo-TEM image of the observed structures at a given reaction time, inset: associated SAED pattern; (C) three dimensional volume rendering from a cryo-ET reconstruction shown over a central XY slice from the reconstruction (*t* = 900 s), insets in C: three-dimensional particle surface renderings at selected angles from -45° < 0° < +45°. Full movies of the tomographic reconstruction and additional images can be found in the ESI.

In the Co-system (Figure 2) the observed trends are similar to those for Ni. Firstly (Figure 2B, *t* = 5 s – 900 s), near-spherical particles agglomerate into larger units, and all the involved species are amorphous until 1500 s (see SAED in Figure 2B). Noticeably, the particles at 5 s are highly irregular and smaller than those in the Ni-system (average size Ni: 50 nm compared to average size Co: 35 nm). Again, these agglomerating frameworks progressively condense with increasing reaction times and form larger assemblies up to 1500 s. After *t* = 2100 s, final µm-sized single crystals appeared, showing a highly regular faceted structure with clear diffraction spots in the SAED pattern. Videos of the tomographic reconstruction of the Ni- and Co-PO_4 precursors based on the cryo-TEM micrographs in different orientations are attached in the electronic supplementary information. Based on the pH curves and the cryo-TEM monitoring, the Co-system demonstrates a significantly longer time (~10x factor) to reach reaction equilibrium compared to the pure Ni-system, which is in addition dependent on the initial Co concentration in solution. Looking at the pH measurements of the Co-system, the time to reach an equilibrium pH and its value itself change starkly after increasing the metal concentration over > 0.04 mol/l (MP > 0.4) [*t* = 500 s for ($c(Co^{2+})$ = 0.02 mol/l, MP = 0.2, pH_{eq} = 5.6 to *t* = 3500 s for $c(Co^{2+})$ = 0.04 mol/l, MP = 0.4, pH_{eq} = 4.5]. Here, the kinetics and the decrease in the pH behavior can be explained by a change in the final crystalline product. Specifically, with increasing Co concentration, the crystallization pathway leads to either Co-struvite ($c(Co^{2+})$ < 0.04 mol/l, MP = 0.4, eq. 1) or to Co-phosphate octahydrate ($c(Co^{2+})$> 0.04 mol/l, MP = 0.4, eq. 2) [4]. Consequently, the increasing Co^{2+} concentration induces a shift towards lower values in the pH curves at around MP ≈ 0.4 [4, 28, 54] (ESI: Figure S1-S3). Since the

Ni-system always leads to Ni-struvite regardless of the metal concentration, the pH trends for this system exhibit practically constant final values (ESI: Figure S1). Based on the multistep patterns observed in the pH curves and the transformation of the three-dimensional framework of the intermediate phases, we assume a complex interplay among amorphous and crystalline solids, and possibly smaller species in solution in the form of (aqueous) clusters.

Time-resolved crystallization of the pure systems: from ions to amorphous phases and to a final crystalline facet

From the results including time-resolved pH measurements, visual observations, and cryo-TEM imaging, we correlated information about the morphology and structure of the transitional nanophases with the specific moments in time. However, such *ex-situ* quenching approach is limited by the realistically achievable time resolution and the number of samples that can be analyzed with electron microscopy. To gain more insights into the as-observed crystallization pathways, we wanted to simultaneously correlate the *in-situ* morphological information, with the temporal phase composition and reaction kinetics. This was achieved by using *in-situ* approaches, avoiding any potential artifacts *e.g.* from quenching. Therefore, *in-situ* scattering (combined SAXS and WAXS) and pH measurements were performed to follow crystallization (see Methods: *In-situ* SAXS/WAXS). In this way, global information about the occurrence of crystalline phases, the presence and size of agglomerates with their building units could be quantified.

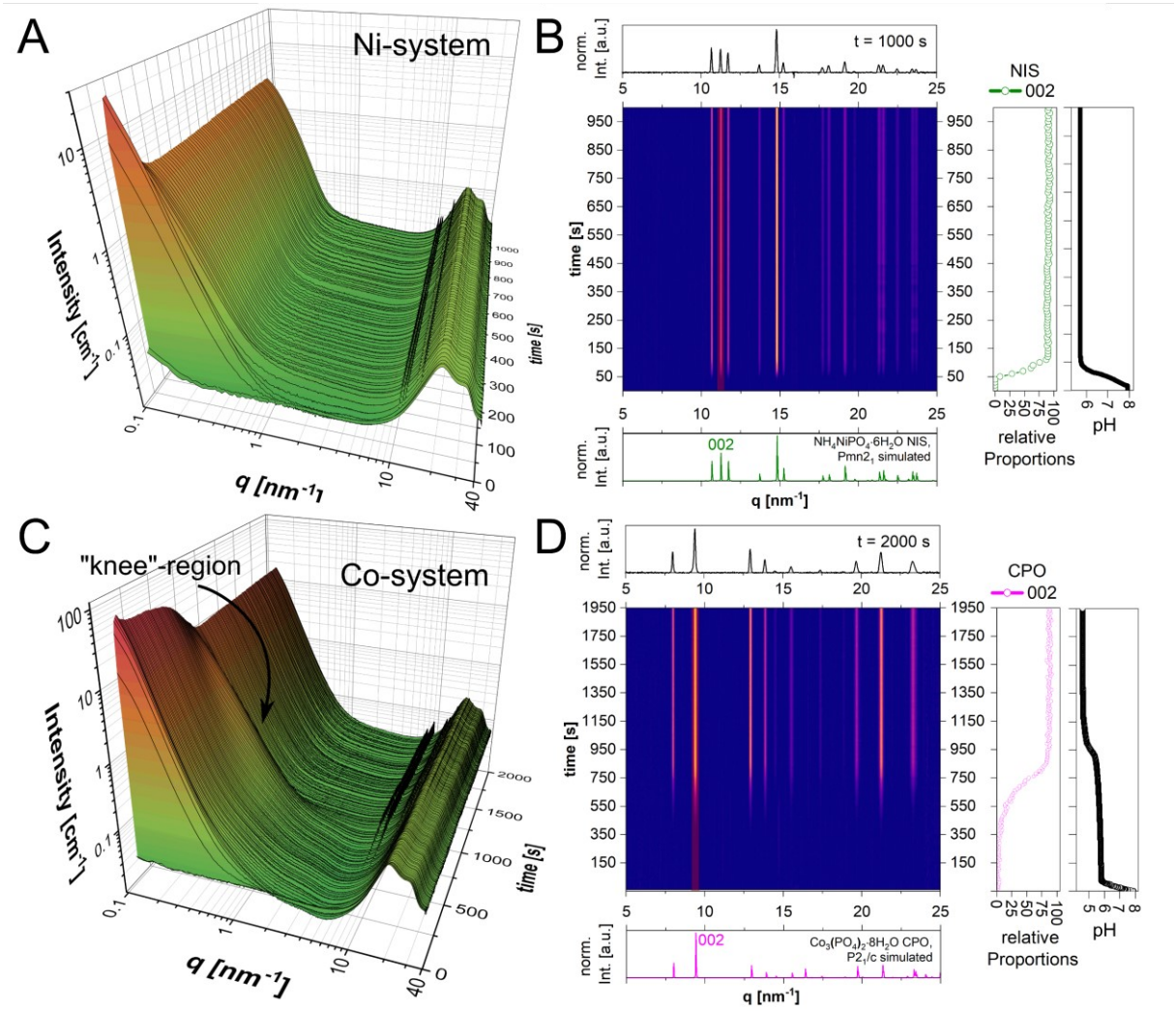

[i]Figure 3: *In-situ* SAXS/WAXS data from crystallization experiments measured with a flow-through setup (ESI: Figure S6) of the pure Ni-system and of the Co-system. In (A) the entire scattering data are displayed in a three-dimensional surface diagram through time while in (B) the WAXS data are summarized in heatmaps for the Ni-system. In (C) the entire scattering data are displayed in a three-dimensional surface diagram through time while in (D) the WAXS data are summarized in heatmaps for the Co-system. The low-intensity SAXS curves at the beginning represent the pre-mixed stage of the pure DAP solution before injection of the metal-bearing solution. WAXS heatmaps: normalized WAXS intensities plotted with simulated crystal structures and the final WAXS signal of the experiment. On the right side: normalized intensity of a characteristic (002) reflection of crystalline phase and simultaneously measured *in-situ* pH data. (NIS = Ni-struvite, CPO = Co-phosphate octahydrate) marked with a red frame. Ni-struvite reference ICSD 403058, Co-phosphate octahydrate COD reference 2020362. SAXS data: Projection of time-resolved normalized SAXS data with colored intensity.

Based on the occurrence of diffraction reflections in the pure Ni-system (Figure 3A, B), Ni-struvite precipitates rapidly for $t < 100$ s as the sole crystalline phase. In the low-q region, at $t < 100$ s after the injection of the metal-bearing solution, the scattering signal is dominated by a high intensity scattering pattern, which implies the presence of large particles of the Ni-struvite crystals manifesting themselves merely as a q^{-4} intensity dependence [56] (Porod interface). In contrast, Co phosphate octahydrate precipitated much slower at $t > 600$ s, while characteristic signal from the primary building units and their agglomerates was visible in the SAXS for $q < 1$ nm^{-1} (Figure 3B, C). Here, a so-called “knee”-region can be identified with its centroid at around 0.4 nm^{-1} indicating potentially polydisperse form factors of nucleating

entities with different sizes (marked with arrow in Figure 3). The precipitation of the actual crystals was completed only at $t > 1500$ s, evidenced by reaching an equilibrium pH of 4.7, the reduction of scattering intensity between 0.3 - 5 nm^{-1} and the development of a Porod interface.

For quantitative analysis and the extraction of the microstructural descriptors, the SAXS part of the scattering data (*i.e.* for 0.1 $nm^{-1} < q < 3$ nm^{-1}) was fitted with a unified model by Beaucage *et al*.[57, 58] (ESI: Supplementary Note 2, eq. S3). A complete description of the model can be found in the ESI (ESI: Supplementary Note 2, Figure S7-S10). From the SAXS fits, significant parameters are used for a system which assumes two distinct structural levels (smaller level denoted as *sub*), and thereby we obtained B, G, G_{sub}, B_{sub}, R_g and R_{sub} as a function of time (ESI: Figure S7). In a nutshell, B and G values are Porod and Guinier pre-factors, accordingly, while R values are radii of gyration. These variables parameterize the scattering profile throughout the considered *q* region. While R_g and R_{sub} are effectively limited by the measured *q*-range, the other parameters exhibit approximately different ranges *e.g.* G ≈ n100 cm^{-1}, G > G_{sub} > n10^{-6} cm^{-1} (with n = 1, 2, 3 …), B and B_{sub} are mostly below 1. The p and p_{sub} parameters show values between 4 and 2, dependent on the interface of the scatterers (p = 4 for sharp, smooth Porod interfaces).

For the Ni-system (ESI: Figure S8), the evolution of the fitting parameters reflects a quick formation of µm-large particles preceded by a fast conversion of the short-lived amorphous phases $t < 100$ s (ESI: Figure S8). Here, the crystallization of Ni-struvite was manifested itself in increasing G and G_{sub} values originated by the slope increase of the SAXS curves at low *q* near 0.1 nm^{-1} (affecting G) and the broad "hump" at around 0.4 nm^{-1} (affecting G_{sub}) (ESI: Figure S8). After the formation of Ni-struvite crystals, all parameters reach a plateau value (ESI: Figure S8).

In contrast, in the Co-system (ESI: Figure S9), the presence of persisting long-lived amorphous phases is manifesting itself by increasing G, B_{sub}, and G_{sub} values indicative of the presence of small building blocks and their agglomerates up to $t = 500$ s (ESI: Figure S9). After $t = 500$ s these parameters decrease sharply, correlating with the development of diffraction reflections which correspond to Co-octahydrate. This suggests that the crystallization is driven by consumption of the amorphous phases. Indeed, we observed the co-existence of amorphous phases together with crystals in cryo-TEM analysis (Figure 2). After around $t = 600$ s a plateau value is reached in most parameters, indicating the equilibration of the precipitation process.

The complex anomalous-behaving Ni_xCo_{1-x}-system

Interestingly, when both metals, *i.e.* Co and Ni, are mixed, the crystallization pathways become even more complex, deviating from the individual trends characteristic of the pure systems.

Ni-struvite crystals formed fast within $t < 100$ s, while Co-phosphate octahydrate crystals were firstly observed after $t > 600$ s. Although we observed slightly contrasting kinetics among the used approaches (*e.g.* see time axis in ESI: Figure S2 and (Ni) S8/ (Co) S9), the differences can be explained by changes in the hydrodynamic regime between the setups (confinement,

pumping rate, etc.). We can conclude that Ni-phosphate demonstrates significantly faster crystallization/transformation kinetics than Co-phosphate. However, both elements precipitate into analogous struvite crystal structures, at least at low M/P ratios, although the pathways are clearly not identical. The Co-system is potentially affected by the presence of long-living metal clusters, indicated by the long-term plateau value in pH at 5.7 and the delayed color change of the solution (Figure 2A, ESI: Figure S2).

The question arose how a mixed-metal system evolves towards crystalline solid solutions. We initially hypothesized that the development rate would be within the limits established by pure metal systems. As a result, compositions containing more Ni would develop faster than those with more Co.

In contrast, the time for completion of the reaction increased strongly and differed significantly from the behavior of the two individual endmembers. We considered several Ni:Co ratios (Ni# = 20, 50, 80) at several concentrations (c(M) = 0.02 M, 0.1 M, 1 M). In this regard, the most counterintuitive mixture was the 50:50 one that exhibited the longest equilibration times (ESI: Figure S2E). This anomalous non-linear (related to the Ni#) trend is further pronounced at very high concentrations of 1 M of the reactants, where the $Ni_{0.5}Co_{0.5}$-system required 6 h to complete, while the pure endmembers needed at most less than one quarter of this time (ESI: Figure S2E and 2F).

The case of the $Ni_{50}Co_{50}$-mixture with its counter-intuitively long reaction time (ESI: Figure S2E and S2F) arose the question of how the reconfiguration of the precursor to a final crystalline unit is accomplished in this system. For this purpose, the $Ni_{50}Co_{50}$-system was also studied with *in-situ* scattering accompanied by pH measurements to observe potential differences in their crystallization pathway.

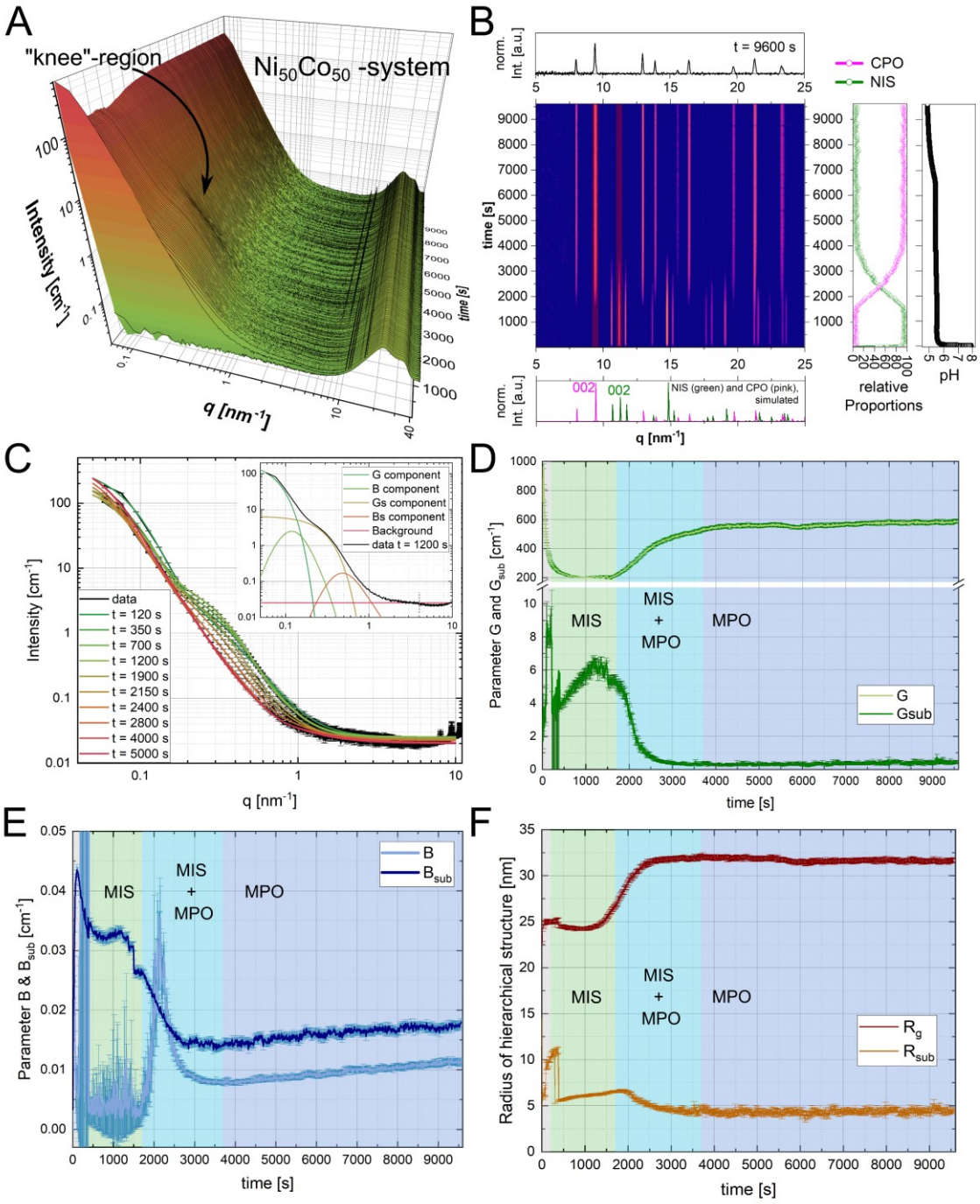

Figure 4: *in-situ* scattering data and fits of the mixed $Ni_{50}Co_{50}$-system: (A) Time-resolved *in-situ* SAXS data with color-marked intensities: low-intensity SAXS curves at the beginning represent the pre-mixed stage of the pure DAP solution before injection of the metal-bearing solution. (B) WAXS heatmaps: normalized WAXS intensities plotted with simulated crystal structures and the final WAXS signal of the experiment. On the right side: normalized Intensity of a characteristic (002) reflection of crystalline phase and simultaneously measured *in-situ* pH data. (NIS = Ni-struvite, CPO = Co-phosphate octahydrate) marked with a red-shadowed frame. Ni-struvite reference ICSD 403058, Co-phosphate octahydrate COD reference 2020362.SAXS data: Projection of time-resolved normalized SAXS data with colored intensity. (C-F) Fitting results of the *in-situ* SAXS data of the $Ni_{50}Co_{50}$-experiment based on a Beaucage model (Supplementary Note 2, eq. S1); (C) Selected fits are displayed and show a good agreement with the data within the error bars; inset: component analysis of the fitting function following eq. S1. Temporal evolutions of selected fitting parameters are presented in the panels (D-F): (D) G and G_{sub}, (E) B and B_{sub}. (F) R_g and R_{sub} in [nm]. The different color shadings mark the distinct phase composition at a given time based on WAXS: grey= no crystalline phases, light green= MIS (Ni_xCo_{1-x}-struvite), blue= MPO (M-phosphate octahydrate), cyan= both.

In theory, both metals can be incorporated into the crystalline phases considered to form solid solutions [4, 5]. However, upon precipitation from aqueous solution, the starting aqueous ionic concentrations and the final metal composition in the crystals differ significantly. Therefore, the occurring crystalline phases are named, M-struvite and M-octahydrate with M = Ni_xCo_{1-x}. In the mixed system, surprisingly, the overall time scales of the entire formation process got extended significantly, and in addition, more complex transformation pathways were observed, including several crystalline phases. Firstly, even faster than in the case of the Ni-system, M-struvite formed within t = 100 s as observed in diffraction and correlating well with the occurrence of q^{-4} interfaces at low angles. Simultaneously, co-existing amorphous phases scattered in the intermediate q region in a "knee" region at around 0.3 nm^{-1} to 1 nm^{-1} similar as in the pure Co-system (Figure 3E and Figure 3F). These scattering features of the amorphous phases evolved through time reaching an intensity maximum at t = 1300 s. In the time interval from 1300 s < t <1700 s, until the first formation of M-octahydrate, the signal at intermediate q decreased rapidly. In the time window from t = 1700 s – 3700 s, the previously formed M-struvite and the M-octahydrate crystals coexisted together. Here, the octahydrate's diffraction intensities increased further, indicative of a growing volume fraction of this phase, while the M-struvite crystals dissolved gradually as evidenced from the disappearance of the associated Bragg peaks. After t = 3700 s, M-struvite was dissolved completely resulting in a single-phase composition of M-octahydrate. Based on the pH curve, equilibrium was reached after the precipitation of M-octahydrate hinted by a drop of pH beginning at t = 6500 s finalized at t = 9000s, to reach a plateau value of 4.7. All significant events in the *in-situ* scattering of the $Ni_{50}Co_{50}$-experiment are summarized in selective time frames (ESI: Figure S7). In the $Ni_{50}Co_{50}$ system, complex trends of the fitting parameter can be observed (Figure 4, ESI: Figure S10). Firstly, at around t = 100 s, the sub-level parameters reached their maximum values (G_{sub} = 9 cm^{-1}, B_{sub} = 0.044 cm^{-1} and R_{sub} = 11 nm) indicative of reaching a maximum number of nucleating entities with several nm in size (ESI: Figure S10). Due to the partial consumption of these building blocks in the Ni-struvite crystal formation, all sub-parameters decreased roughly by half until t = 400 s (G_{sub} = 4 cm^{-1}, B_{sub} = 0.033 cm^{-1} and R_{sub} = 5.5 nm, ESI: Figure S10). In contrast, the hierarchically higher-level parameters G, B, and R_g declined rapidly to a minimum value (G = 200 cm^{-1}, B = 0.005 cm^{-1} and R_g = 24 nm). Concurrently, the R_{sub} of the nucleating entities grew progressively by around 15% to around 7 nm until t = 1900 s (Figure 4F). When the dissolution of M-struvite (MIS) started, all sub-parameters declined to a global minimum. As R_{sub} is most likely representing the radius of the smallest characteristic entity, it also declined to a constant plateau value. It is just affected by B_{sub} (G_{sub} ≈ 0 cm^{-1}) and, therefore, the signal extinguishes after their consumption. Consequently, the evolution and absolute values of R_g are congruent and in the same length scale to the sizes of the spherical building units observable in the TEM micrographs. Due to the simultaneous co-precipitation of M-phosphate octahydrate (MPO), the higher-level parameters G and R_g increased to a plateau value with R_g = 32 nm and G = 580 cm^{-1} at around t = 3000 s. Most likely even larger particles form could not be quantified sufficiently well from the model as the lower q-range would be required. B is deviating from this trend as it is affected by R_g and R_{sub} (ESI: Supplementary Note 2).

In sum, the fits of the *in-situ* SAXS data reflect the nucleation of the precursors, its entities and the transformation processes between them. The *in-situ* scattering data clearly demonstrate

the coexistence of amorphous precursors and already formed crystalline phases in several time intervals.

In the pure-metal system, we observed a progressive transformation from amorphous to crystalline compounds. Based on this finding, we assumed that the formed crystals were the thermodynamically favored phases *i.e.* Ni- or Co-struvite. However, the mixed Ni_xCo_{1-x} experiments showed the opposite. Here, amorphous precursors coexist with crystalline phases over a long period, while the first precipitated crystals are unstable and "consumed" by a later forming crystalline phase.

Our results suggest that the reaction pathway is controlled by the type and concentration of the transition metal cation(s). Ni and Co can form the same isostructural crystalline phases, namely M-struvite and M-octahydrate. Therefore, looking at the final crystalline solids, one would also expect isostructural TMP solid solutions including both metals. However, the observed complex non-classical crystallization pathways of the considered TMPs suggest that the incorporation of both metals into crystals would be driven by very different kinetic rates and thermodynamic equilibria of different multi-step mechanisms. In this regard, the starting concentration of metals in solution is unlikely to reflect the metal concentration in the crystalline phases. Considering this hypothesis, in the further characterization, we explored if indeed any elemental fractionation occurred in the mixed Ni_xCo_{1-x} experiments between Ni and Co in their solid solutions. Therefore, to explain this aspect and to quantify the temporal elemental participation of P, Co, and Ni during the precipitation, we analyzed the chemical composition of the solid phases and the associated supernatants from different stages with ICP-MS. Although the measurements were essentially *ex-situ*, we used the same flow-through setup as with the scattering experiments to synthesize TMPs to ensure near-direct comparability among various approaches, evidenced also by matching the pH trends (ESI: Figure S11, Table S3)

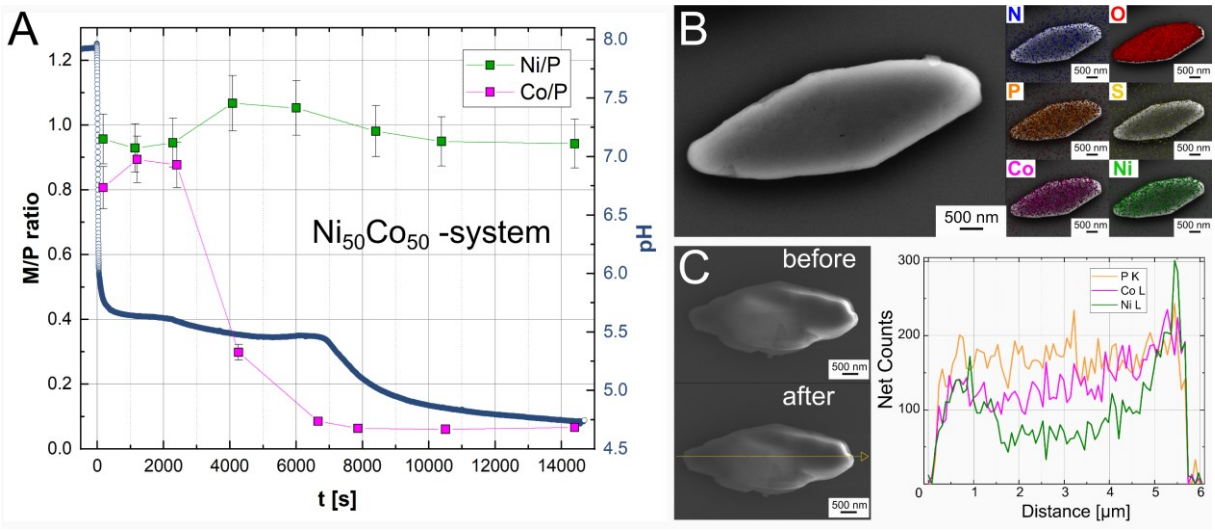

Figure 5: (A) *ex-situ* ICP-MS data plots displayed in mass ratios Ni/P and Co/P with error of two standard deviation (95.7%) and simultaneously measured *in-situ* pH curve. (B) SEM/EDS elemental maps and (C) SEM/EDS line scan of a single crystal of $Ni_xCo_{1-x}(PO_4)_2{\cdot}8H_2O$ with elemental distribution of N, O, P, S, Co and Ni, and SE images before and after the measurement.

The ICP-MS data of the mother supernatant correlate with the observations of the *in-situ* experiments (Figure 4, ESI: Table S3). In the first seconds, Ni- and Co-PO_4 co-precipitated near equally, as it is visible in comparable MP ratios of around 0.9 (Figure 5A). From scattering we learned that M-struvite formed quickly, while the amorphous phases began to agglomerate (Figure 3 and Figure 4, ESI: Table S3). Until around t = 3000 s the Ni/P remained constant, while the Co/P ratio showed a slight increase of around 10% overall (Figure 4A). In this period, M-struvite and amorphous nanophases formed, as was indicated by the plateau value of the pH and the increasing sub-parameters in scattering (Figure 4, ESI: Figure S1-S3, Table S3). After t = 3000 s the simultaneous dissolution of the primary M-struvite and the precipitation of M-phosphate octahydrate, resulted in a slightly increasing Ni/P ratio and starkly falling Co/P ratio. Based on the increasing G and R_g scattering parameters and the elemental analysis, the formation of the M-phosphate octahydrate crystals occurred gradually over two to three thousand seconds. At this stage, Ni was released slightly ≈ +15 % into the solution resulting in a Ni/P ratio of ≈ 1.05, while Co was almost completely ≈ -90% (decreasing Co/P ratio in the solution ≈ 0.05) incorporated in a solid phase (Figure 4A). Importantly, M-phosphate octahydrate had a higher MP = 1.5 than M-struvite with MP = 1, and therefore the absolute phosphate content increased after dissolution of M-struvite. Finally, after extended reaction times of t = 8000 s, the Ni/P ratio declined to a constant value of 0.9 reflecting only a partial incorporation of Ni into the M-phosphate octahydrate crystals. Most of the Co content was precipitated in $M_3(PO_4)_2{\cdot}8H_2O$ crystals, resulting in low remaining absolute Co content in the solution. Based on the EDS mappings, line scans, and bulk ICP-MS data from different Ni_xCo_{1-x} mixtures (x = 0.3, 0.5, and 0.7), we observed an extensive trend of metal fractionation during the formation of M-phosphate octahydrate (Figure 4B). The calculated Ni# from EDS analysis of the mapped $M_3(PO_4)_2{\cdot}8H_2O$ crystals were significantly lower than the Ni# in the solution (ESI: Figure S14). Furthermore, in the EDS line scans, a slight zonation of Ni in the Co-rich samples could be identified (Ni# >0.5) in the M-phosphate octahydrate crystals (Figure 4C). Here, Ni was concentrated in the outer rims while the cores of the crystals were enriched in Co, respectively to each other. In addition, the calculated Ni# from bulk ICP-MS data agreed well with the EDS data (ESI: Table S4). Thus, the fractionation of Ni and Co occurred in all crystals, following the same temporal and spatial patterns of the elemental distribution. Interestingly, in the Ni_xCo_{1-x}-mixture with x = 0.8, where M-struvite was also present at the end of the reaction with M-phosphate octahydrate in a binary phase mixture (ESI: Figure S1), the calculated Ni# agreed with the Ni# in the solution (ESI: Figure S13, Figure S14, Table S2).

The transformation of the amorphous precursor and reaction kinetics of transition metals

The occurrence of intermediate amorphous nanophases in the pure and mixed metal systems, followed by their restructuring and densification, demonstrated a multi-step crystallization route. Therefore, the TMPs crystallization is non-classical. Although the amorphous intermediate phases formed quickly in the early reaction stages, their reconfiguration and aggregation occurred gradually over many seconds to minutes. After a threshold density and µm-size of the agglomerates were reached, the final transformation to a crystal seemed to be

very fast. Since the actual transformation to a crystalline material occured within seconds and exhibited highly stochastic characteristics, it proved challenging to be tracked with *ex-situ* approaches. Namely, transitional amorphous phases and final crystals can coexist within a limited metastable time window. Interestingly, neither individual nanocrystals nor standalone spherical building units were found in the samples. Instead, we observed only larger mesoscopic agglomerates of building units, or already crystals of µm-size. This suggests that the outcome of TMPs crystallization should be potentially controllable by confinement/finite volume [59]. We speculate that the occurrence and the stability of the amorphous phases is actually controlled by meta-stable, but long-living aqua ammonia complexes ($M^{2+}(H_2O)_x(NH_3)_{1-x}$) present in solutions, whose evolution affects the equilibria of the evolving solids [60, 61]. They may have an impact on crystallization *i.e.* on the formation of nm-sized clusters by decreasing the amount of available free Ni^{2+}, Co^{2+} or NH_4^+ ions. Such speciation-dependent, solid vs. aqueous cluster equilibria would explain very different transformation kinetics of the amorphous phase agglomerates, including the anomalous evolution in the mixed-metal systems. Another kinetic reason to consider, in the light of the evolution of pH trends, are associated stabilities of different protonated phosphate species. Starting pH ≈ 8, such conditions would stabilize predominantly the single protonated HPO_4^{2-} species while at the end of precipitation the drop in pH to 4.6 would shift the equilibrium to the double protonated $H_2PO_4^-$. The presence of different protonated phosphate ligands in an aqueous solution could potentially affect the local structure of strongly hydrated amorphous transition metal phosphate nanophases - analogously observed in calcium-carbonate and -phosphate systems [62-64]. They could form similar frameworks as observed structures of Posner clusters in the crystallization pathway of apatite [65, 66].

Growth of crystalline phases

Since the TMPs crystallization pathways are multi-step, consequently, the reaction kinetics of the TMPs precipitation is primarily dependent on the stability of the amorphous precursors and their agglomerates, and to a lesser extent on the final crystallization step. However, this "final" transformation ought to be also considered. Looking at the solubility product *i.e.*, the thermodynamic driving force for precipitation, the K_{sp} of M-struvite is magnitudes higher compared to the one of M-phosphate octahydrate at ambient conditions [67, 68]. However, M-struvite still demonstrates the faster reaction kinetics compared to M-phosphate octahydrate. This could be explained by crystallographic differences in the transition metal phosphate structures. Based on the cryo-TEM and *in-situ* scattering data, we could indeed extract the information about phase, morphology and key differences in the evolving frameworks of the amorphous phases and their transformation to crystalline solids depending on the involved transition metals. While we focused in the previous part of discussion on the stability and the effects of the amorphous phases, we consider further the evolution of the occurring crystal structures, namely M-struvite and M-phosphate octahydrate. From a crystallographic point of view, as Co-phosphate octahydrate exhibits large d_{hkl} of the (110) and (002) plane, due to its layered structure (Figure 3 Figure 4, q_{110} or q_{002} < 10 nm^{-1}), these crystal planes exhibit

resulting high load densities and growth velocities. This is the reason why these planes have a large probability to form and scatter with high intensity (as is concluded from Bravais-Friedel-Donnay-Harker model) [69, 70]. As it can be seen in Figure 3, in M-struvite the intensity of the (101), (002), and (011) reflections increases immediately, while the (110) and (020) reflections of M-phosphate octahydrate grow gradually due to their layered nature. The fast formation kinetics of M-struvite compared to M-phosphate octahydrate are probably related to its simple crystallographic structure of isolated building units, mainly the isolated phosphate tetrahedron and isolated metal octahedron coordinated by crystal water [4, 54, 71]. However, the Co-phosphate octahydrate structure is more complex depicted for example in the occurrence of two different metal sites. In the first site, the transition metal is surrounded by four water molecules and two oxygen atoms, resulting in the octahedron $Co(H_2O)_4O_2$. In the second site, the transition metal is coordinated by two water molecules and four oxygen atoms, leading to $Co(H_2O)_2O_4$. The (110) reflection of M-phosphate octahydrate represents the crystal plane constructed by a regular arrangement of octahedral $Co(H_2O)_4O_2$ or $Co(H_2O)_2O_4$ units with a d-spacing of d_{110} = 7.83 Å, whereas the (020) reflection lies in the plane of linked Co octahedrons (both types) with tetrahedral coordinated PO_4 phosphate units with a d-spacing of d_{020} = 6.67 Å. Firstly, the crystal structure is most likely to build up in one c-layer by the arrangement of disordered super units of linked Co-octahedrons and PO_4 tetrahedrons resulting in the presence of the (110) and (020) reflections. Here 00ℓ reflections would not occur as the layers are internally disordered and grow in single layers. At extended reaction time, additional layers begin to form in the c-direction. Here, inside the c-layer the $Co(H_2O)_4O_2$ and PO_4 self-assemble and reach a higher degree of ordering resulting in the appearance of (200) [d_{200} = 4.84 Å], (001) [d_{001} = 4.52 Å] and other reflections. A visualization of the lattice planes in the crystal structure of Co-phosphate octahydrate is depicted in the ESI (ESI: Figure S15).

The actual accomplishment of the transformation in the solid, from a disordered, amorphous to an ordered, crystalline state in the solid compounds is still not well-understood, either in phosphates or in other mineral systems. For instance, this issue of a stochastic 'jump' of a dense agglomerate to a primary crystal is also debated [72 62, 73]in other material classes such as the conversion of amorphous calcium carbonate (ACC) to a crystalline carbonate[74, 75] or in the calcium sulfate system[51]. However, we assume that the amorphous highly agglomerated solid exhibits at least a certain short-range order. Indicators for this assumption could be the fast transformation to a crystal within seconds, while the process of agglomeration and densification of the primary building blocks required more time, from minutes to hours. By slightly ordering the disordered c-layers in M-phosphate octahydrate or isolated building units (NH_4, PO_4, MO_6) in M-struvite, the previously amorphous solid could establish a three-dimensional periodic crystalline order in the compound. Thus, the primary nucleating crystal would form.

Conclusion

We revealed how transition metal phosphates form crystals through a non-classical pathway that involves temporary, amorphous particles on the way to the final crystal. These amorphous phases undergo various stages of aggregation, densification, and reconfiguration

to proto-crystalline precursors varying considerably depending on the transition metal(s) involved. The reaction kinetics of the precipitation of TMP phases is primarily dependent on the involved transition metal(s), the stability properties of the amorphous precursors and their agglomerated entities. Additionally, the rate of formation is affected by the complexity of the final crystalline structure (layered vs. isolated structure). When combining Ni and Co equally in high concentration, the time it took to reach equilibrium was significantly prolonged, from a few minutes to several hours, providing evidence of the intricate interaction between transition metal ions and potential complexes, and the nucleating solid entities.

Electronic Supplementary Information

An electronic supplementary information file for this work is available. It contains the following items:

Methods: X-ray diffraction, pH measurements, Infrared spectroscopy, SEM/EDS, Conventional TEM, Cryo-TEM, In-situ SAXS/WAXS, ICP-MS,

Figures: Figure S1: Stacked diffractograms of synthesized Ni, Co and Ni_xCo_{1-x} phosphate samples, Figure S2: Time-resolved pH data of different reaction runs of Ni, Co and Ni_xCo_{1-x} with x = 20%, 50%, 80% phosphates in varying concentrations, Figure S3: Conventional TEM micrographs of Ni- and Co phosphates with BF image and associated EDX maps of the precursor Ni- or Co-phosphate phases, Figure S4: Cryo-TEM analysis and tomographic reconstructions of the amorphous Ni- and Co phosphate nanophases displayed in different angles, Figure S5: Fourier transform-infrared (FT-IR) spectra of crystalline Ni_xCo_{1-x}- samples, Figure S6: Flow-through-setup sketch, Figure S7: Selected time frames in scattering/diffraction of the mixed $Ni_{50}Co_{50}$ experiment and component analysis of the fit function, Figure S8: Fitting results of the in-situ SAXS data of the Ni-experiment based on a Beaucage model, Figure S9: Fitting results of the in-situ SAXS data of the Co-experiment based on a Beaucage model, Figure S10: Fitting results of the in-situ SAXS data of the mixed $Ni_{50}Co_{50}$-experiment based on a Beaucage model, Figure S11: ICP-MS data of the particle-filtered solution with triplicate runs in absolute mass fractions, Figure S12: EDS maps of analyzed Ni_xCo_{1-x} solids with x = 0.1-0.9, Figure S13: EDS-Line Scans of analyzed Ni_xCo_{1-x} solids with x = 30, x = 50 and x = 80 in the experiment, Figure S14: ICP-MS data of Ni, Co and P and comparison of elemental information obtained by ICP-MS and the EDX maps of multiple grains, Figure S15: Crystal structures of M-struvite $Pmn2_1$ and M-phosphate octahydrate C2/m,

Tables: Table S1: Settings of the ICP-MS instrument used for the quantification, Table S2: Summarized EDS data from multiple maps of Ni_xCo_{1-x}-phosphate octahydrate crystals with weight and atomic percentage of the respective element, Table S3: ICP-MS data of particle-filtered solution from crystallization experiments in triplicate runs, Table S4: ICP-MS data of dissolved $(Ni_xCo_{1-x})_3(PO_4)_2$ crystals in triplicate runs,

Supplementary Notes: Supplementary Note 1: pH curves as a proxy for reaction progress, Supplementary Note 2: Fitting SAXS data with a simplified Beaucage model.

Videos: Supplementary Video 1 *movie_Ni_300_s.avi* : 3D tomographic reconstruction of the Ni-PO_4 precursor phases at t = 300 s derived from cryo-TEM micrographs is shown in different orientations ($-60° < \theta < 60°$). 360° rotation of the reconstructed object around the z-axis in the

x-y-plane, Supplementary Video 2 *movie_Co_600_s.avi* : 3D tomographic reconstruction of the Co-PO_4 precursor phases at t = 600 s, derived from cryo-TEM micrographs is shown in different orientations (-60° < θ < 60°). 360° rotation of the reconstructed object around the z-axis in the x-y-plane.

Data availability

The data that support the findings of this study are available from the corresponding authors upon reasonable request.

Conflict of Interest

The authors have no conflicts to declare.

Acknowledgements

We thank BAM and Helmholtz-Zentrum Berlin (HZB) for providing beamtime at mySpot of BESSY II. In addition, we thank Helmholtz-Zentrum Berlin (HZB) for providing access to the electron microscopes.

References

1. Gislev, M.; Grohol, M.; Mathieux, F.; Ardente, F. *Report on Critical Raw Materials in the Circular Economy*; European Commission: 2018.
2. Cordell, D.; Drangert, J.-O.; White, S., The story of phosphorus: Global food security and food for thought. *Global Environmental Change* **2009,** *19* (2), 292-305.
3. Filippelli, G. M., The Global Phosphorus Cycle. *Reviews in Mineralogy and Geochemistry* **2002,** *48* (1), 391-425.
4. Karafiludis, S.; Buzanich, A. G.; Kochovski, Z.; Feldmann, I.; Emmerling, F.; Stawski, T. M., Ni- and Co-Struvites: Revealing Crystallization Mechanisms and Crystal Engineering toward Applicational Use of Transition Metal Phosphates. *Crystal Growth & Design* **2022,** *22* (7), 4305-4315.
5. Karafiludis, S.; Buzanich, A. G.; Heinekamp, C.; Zimathies, A.; Smales, G. J.; Hodoroaba, V.-D.; ten Elshof, J. E.; Emmerling, F.; Stawski, T. M., Template-free synthesis of mesoporous, amorphous transition metal phosphate materials. *Nanoscale* **2023,** *15* (8), 3952-3966.
6. Mohammed, H.; Al-Othman, A.; Nancarrow, P.; Elsayed, Y.; Tawalbeh, M., Enhanced proton conduction in zirconium phosphate/ionic liquids materials for high-temperature fuel cells. *International Journal of Hydrogen Energy* **2021,** *46* (6), 4857-4869.
7. Huang, W.; Komarneni, S.; Noh, Y. D.; Ma, J.; Chen, K.; Xue, D.; Xue, X.; Jiang, B., Novel inorganic tin phosphate gel: multifunctional material. *Chem Commun (Camb)* **2018,** *54* (21), 2682-2685.
8. Karafiludis, S.; Bhattacharya, B.; Buzanich, A. G.; Fink, F.; Feldmann, I.; ten Elshof, J. E.; Emmerling, F.; Stawski, T. M., Thermally processed Ni-and Co-struvites as functional materials for proton conductivity. *Dalton Transactions* **2023,** *52* (24), 8262-8274.

9. Zhao, Y.; Chen, Z.; Xiong, D. B.; Qiao, Y.; Tang, Y.; Gao, F., Hybridized Phosphate with Ultrathin Nanoslices and Single Crystal Microplatelets for High Performance Supercapacitors. *Sci Rep* **2016,** *6*, 17613.
10. Lin, J.; Chen, N.; Pan, Y., Arsenic incorporation in synthetic struvite (NH4MgPO4.6H2O): a synchrotron XAS and single-crystal EPR study. *Environ Sci Technol* **2013,** *47* (22), 35-12728.
11. Xu, X.; Du, P.; Guo, T.; Zhao, B.; Wang, H.; Huang, M., In situ Grown Ni phosphate@Ni12P5 Nanorod Arrays as a Unique Core–Shell Architecture: Competitive Bifunctional Electrocatalysts for Urea Electrolysis at Large Current Densities. *ACS Sustainable Chemistry & Engineering* **2020,** *8* (19), 7463-7471.
12. Meguerdichian, A. G.; Jafari, T.; Shakil, M. R.; Miao, R.; Achola, L. A.; Macharia, J.; Shirazi-Amin, A.; Suib, S. L., Synthesis and Electrocatalytic Activity of Ammonium Nickel Phosphate, [NH4]NiPO4.6H2O, and beta-Nickel Pyrophosphate, beta-Ni2P2O7: Catalysts for Electrocatalytic Decomposition of Urea. *Inorg Chem* **2018,** *57* (4), 1815-1823.
13. Septiani, N. L. W.; Kaneti, Y. V.; Fathoni, K. B.; Kani, K.; Allah, A. E.; Yuliarto, B.; Nugraha; Dipojono, H. K.; Alothman, Z. A.; Golberg, D.; Yamauchi, Y., Self-Assembly of Two-Dimensional Bimetallic Nickel–Cobalt Phosphate Nanoplates into One-Dimensional Porous Chainlike Architecture for Efficient Oxygen Evolution Reaction. *Chemistry of Materials* **2020,** *32* (16), 7005-7018.
14. Song, Z.; Wang, K. C.; Sun, Q.; Zhang, L.; Li, J.; Li, D.; Sze, P. W.; Liang, Y.; Sun, X.; Fu, X. Z.; Luo, J. L., High-Performance Ammonium Cobalt Phosphate Nanosheet Electrocatalyst for Alkaline Saline Water Oxidation. *Adv Sci (Weinh)* **2021,** *8* (14), 2100498.
15. Zhao, H.; Yuan, Z., Insights into Transition Metal Phosphate Materials for Efficient Electrocatalysis. *ChemCatChem* **2020,** *12* (15), 3797-3810.
16. Lin, R.; Ding, Y., A Review on the Synthesis and Applications of Mesostructured Transition Metal Phosphates. *Materials (Basel)* **2013,** *6* (1), 217-243.
17. Huang, H.; Xu, C.; Zhang, W., Removal of nutrients from piggery wastewater using struvite precipitation and pyrogenation technology. *Bioresour Technol* **2011,** *102* (3), 8-2523.
18. El Diwani, G.; El Rafie, S.; El Ibiari, N. N.; El-Aila, H. I., Recovery of ammonia nitrogen from industrial wastewater treatment as struvite slow releasing fertilizer. *Desalination* **2007,** *214* (1-3), 200-214.
19. Münch, E. V.; Barr, K., Controlled struvite crystallisation for removing phosphorus from anaerobic digester sidestreams. *Water Research* **2001,** *35* (1), 151-159.
20. Paskin, A.; Couasnon, T.; Perez, J. P. H.; Lobanov, S. S.; Blukis, R.; Reinsch, S.; Benning, L. G., Nucleation and Crystallization of Ferrous Phosphate Hydrate via an Amorphous Intermediate. *Journal of the American Chemical Society* **2023,** *145* (28), 15137-15151.
21. Zhangchen, R.; Liu, W. G., Q.; ; Ji, H.; Li, Y.; Zhang, J.; Song, J.; Zhong, Y.; Zhou, L., Struvite as seed materials for treatment of heavy metals in wastewater. *IOP Conference Series: Earth and Environmental Science (EES)* **2021,** *770*, 1-5.
22. Rouff, A. A., Sorption of chromium with struvite during phosphorus recovery. *Environ Sci Technol* **2012,** *46* (22), 12493-501.
23. Rouff, A. A.; Juarez, K. M., Zinc interaction with struvite during and after mineral formation. *Environ Sci Technol* **2014,** *48* (11), 6342-9.
24. Lu, X.; Huang, Z.; Liang, Z.; Li, Z.; Yang, J.; Wang, Y.; Wang, F., Co-precipitation of Cu and Zn in precipitation of struvite. *Sci Total Environ* **2021,** *764*, 144269.
25. Ravikumar, R.; Chandrasekhar, A.; Rama Krishnar, C.; Reddy, Y., X-ray powder diffraction, thermal analysis and IR studies of zinc ammonium phosphate hexahydrate. *Optoelectronics and Advanced Materials -Rapid Communciations* **2010,** *4*, 215-219.

26. Abbona, F.; Angela-Frachini, M.; Croni Bono, C.; Lundager Madsen, H. E., Effect of ammonia excess on the crystal habit of NiNH4PO4*6H2O (Ni-struvite). *Journal of Crystal Growth* **1994,** *143*, 256-260.
27. Haferburg, G.; Kloess, G.; Schmitz, W.; Kothe, E., "Ni-struvite" - a new biomineral formed by a nickel resistant Streptomyces acidiscabies. *Chemosphere* **2008,** *72* (3), 517-23.
28. Hövelmann, J.; Stawski, T. M.; Freeman, H. M.; Besselink, R.; Mayanna, S.; Perez, J. P. H.; Hondow, N. S.; Benning, L. G., Struvite Crystallisation and the Effect of Co2+ Ions. *Minerals* **2019,** *9* (9).
29. Hövelmann, J.; Stawski, T. M.; Besselink, R.; Freeman, H. M.; Dietmann, K. M.; Mayanna, S.; Pauw, B. R.; Benning, L. G., A template-free and low temperature method for the synthesis of mesoporous magnesium phosphate with uniform pore structure and high surface area. *Nanoscale* **2019,** *11* (14), 6939-6951.
30. Gibbs, J. W., On the Equilibrium of Heterogeneous Substances. *Transactions of the Connecticut Academy of .Arts and Sciences* **1876,** *3*, 108-248.
31. Volmer, M.; Weber, A., Keimbildung in übersättigten Gebilden. *Zeitschrift für Physikalische Chemie* **1926**, 277-301.
32. Lin, C.; Zhang, Y.; Liu, J. J.; Wang, X. Z., Study on nucleation kinetics of lysozyme crystallization. *Journal of Crystal Growth* **2017,** *469*, 59-64.
33. Auer, S.; Frenkel, D., Numerical prediction of absolute crystallization rates in hard-sphere colloids. *J Chem Phys* **2004,** *120* (6), 3015-29.
34. Kalikmanov, V. I., Effective binary theory of multi-component nucleation. *J Chem Phys* **2015,** *142* (12), 124111.
35. Merikanto, J.; Zapadinsky, E.; Lauri, A.; Vehkamaki, H., Origin of the failure of classical nucleation theory: incorrect description of the smallest clusters. *Phys Rev Lett* **2007,** *98* (14), 145702.
36. Schmelzer, J. W. P.; Abyzov, A. S., Crystallization of glass-forming melts: New answers to old questions. *Journal of Non-Crystalline Solids* **2018,** *501*, 11-20.
37. Gránásy, L.; Iglói, F., Comparison of experiments and modern theories of crystal nucleation. *J Chem Phys* **1997,** *107*, 3634-3644.
38. Oxtoby, D. W., Nucleation of First-Order Phase Transitions. *Accounts of Chemical Research* **1998,** *31* (2), 91-97.
39. Gebauer, D.; Völkel, A.; Cölfen, H., Stable prenucleation Calcium Carbonate Clusters. *Science* **2008,** *322* (5909), 1819-1822.
40. Vekilov, P. G., The two-step mechanism of nucleation of crystals in solution. *Nanoscale* **2010,** *2* (11).
41. Cookman, J.; Hamilton, V.; Hall, S. R.; Bangert, U., Non-classical crystallisation pathway directly observed for a pharmaceutical crystal via liquid phase electron microscopy. *Sci Rep* **2020,** *10* (1), 19156.
42. Warzecha, M.; Florence, A. J.; Vekilov, P. G., The Ambiguous Functions of the Precursors That Enable Nonclassical Modes of Olanzapine Nucleation and Growth. *Crystals* **2021,** *11* (7).
43. Sauter, A.; Oelker, M.; Zocher, G.; Zhang, F.; Stehle, T.; Schreiber, F., Nonclassical Pathways of Protein Crystallization in the Presence of Multivalent Metal Ions. *Crystal Growth & Design* **2014,** *14* (12), 6357-6366.
44. Sauter, A.; Roosen-Runge, F.; Zhang, F.; Lotze, G.; Jacobs, R. M.; Schreiber, F., Real-time observation of nonclassical protein crystallization kinetics. *J Am Chem Soc* **2015,** *137* (4), 1485-91.

45. Sleutel, M.; Van Driessche, A. E., Role of clusters in nonclassical nucleation and growth of protein crystals. *Proc Natl Acad Sci U S A* **2014,** *111* (5), E546-53.
46. Greer, H. F., Non-classical crystal growth of inorganic and organic materials. *Materials Science and Technology* **2014,** *30* (6), 611-626.
47. Tsarfati, Y.; Rosenne, S.; Weissman, H.; Shimon, L. J. W.; Gur, D.; Palmer, B. A.; Rybtchinski, B., Crystallization of Organic Molecules: Nonclassical Mechanism Revealed by Direct Imaging. *ACS Cent Sci* **2018,** *4* (8), 1031-1036.
48. Suk, J.-H.; Hwang, N.-M., Non-classical Crystallization of Bulk Crystals in Solution and of Thin Films in the Gas Phase by Chemical Vapor Deposition. *Electronic Materials Letters* **2021,** *18* (1), 1-26.
49. Jung, J.-s.; Hwang, N.-m., Non-Classical Crystallization of Thin Films and Nanostructures in CVD Process. In *Chemical Vapor Deposition - Recent Advances and Applications in Optical, Solar Cells and Solid State Devices*, 2016.
50. Sear, R. P., The non-classical nucleation of crystals: microscopic mechanisms and applications to molecular crystals, ice and calcium carbonate. *International Materials Reviews* **2013,** *57* (6), 328-356.
51. Stawski, T. M.; van Driessche, A. E.; Ossorio, M.; Diego Rodriguez-Blanco, J.; Besselink, R.; Benning, L. G., Formation of calcium sulfate through the aggregation of sub-3 nanometre primary species. *Nat Commun* **2016,** *7*, 11177.
52. Ruiz-Agudo, E.; Ruiz-Agudo, C.; Di Lorenzo, F.; Alvarez-Lloret, P.; Ibanez-Velasco, A.; Rodriguez-Navarro, C., Citrate Stabilizes Hydroxylapatite Precursors: Implications for Bone Mineralization. *ACS Biomater Sci Eng* **2021,** *7* (6), 2346-2357.
53. Besselink, R.; Stawski, T. M.; Freeman, H. M.; Hövelmann, J.; Tobler, D. J.; Benning, L. G., Mechanism of Saponite Crystallization from a Rapidly Formed Amorphous Intermediate. *Crystal Growth & Design* **2020,** *20* (5), 3365-3373.
54. Karafiludis, S.; Ryll, T. W.; Guilherme Buzanich, A.; Emmerling, F.; Stawski, T. M., Phase stability studies on transition metal phosphates aided by an automated synthesis. *CrystEngComm* **2023**.
55. Midgley, P. A.; Dunin-Borkowski, R. E., Electron tomography and holography in materials science. *Nat Mater* **2009,** *8* (4), 271-80.
56. Besselink, R.; Stawski, T. M.; Van Driessche, A. E. S.; Benning, L. G., Not just fractal surfaces, but surface fractal aggregates: Derivation of the expression for the structure factor and its applications. *The Journal of Chemical Physics* **2016,** *145* (21), 211908.
57. Beaucage, G., Approximations Leading to a Unified Exponential/Power-Law Approach to Small-Angle Scattering. *J. Appl. Cryst.* **1995,** *28*, 717-728.
58. Beaucage, G., Small-Angle Scattering from Polymeric Mass Fractals of Arbitrary Mass-Fractal Dimension. *J. Appl. Cryst.* **1996,** *29*, 134-146.
59. Meldrum, F. C.; O'Shaughnessy, C., Crystallization in Confinement. *Advanced Materials* **2020,** *32* (31), 2001068.
60. van Bommel, A.; Dahn, J. R., Analysis of the Growth Mechanism of Coprecipitated Spherical and Dense Nickel, Manganese, and Cobalt-Containing Hydroxides in the Presence of Aqueous Ammonia. *Chemistry of Materials* **2009,** *21* (8), 1500-1503.
61. Rodríguez-Iznaga, I.; Petranovskii, V.; Rodríguez-Fuentes, G., Ion-exchange of amino- and aqua-complexes of nickel and cobalt in natural clinoptilolite. *Journal of Environmental Chemical Engineering* **2014,** *2* (3), 1221-1227.
62. Wolf, S. E.; Muller, L.; Barrea, R.; Kampf, C. J.; Leiterer, J.; Panne, U.; Hoffmann, T.; Emmerling, F.; Tremel, W., Carbonate-coordinated metal complexes precede the formation of

liquid amorphous mineral emulsions of divalent metal carbonates. *Nanoscale* **2011,** *3* (3), 1158-65.
63. Habraken, W. J.; Tao, J.; Brylka, L. J.; Friedrich, H.; Bertinetti, L.; Schenk, A. S.; Verch, A.; Dmitrovic, V.; Bomans, P. H.; Frederik, P. M.; Laven, J.; van der Schoot, P.; Aichmayer, B.; de With, G.; DeYoreo, J. J.; Sommerdijk, N. A., Ion-association complexes unite classical and non-classical theories for the biomimetic nucleation of calcium phosphate. *Nat Commun* **2013,** *4*, 1507.
64. Lin, T. J.; Chiu, C. C., Structures and infrared spectra of calcium phosphate clusters by ab initio methods with implicit solvation models. *Phys Chem Chem Phys* **2017,** *20* (1), 345-356.
65. Treboux, G.; Layrolle, P.; Kanzaki, N.; Onuma, K.; Ito, A., Symmetry of Posner's Cluster. *Journal of the American Chemical Society* **2000,** *122* (34), 8323-8324.
66. Posner, A. S.; Betts, F., Synthetic amorphous calcium phosphate and its relation to bone mineral structure. *Accounts of Chemical Research* **1975,** *8* (8), 273-281.
67. Madsen, H. E. L., Solubility Product of Ni-Struvite, NH4NiPO4*6H2O, at 25°C. *Advances in Chemical Engineering and Science* **2017,** *07* (02), 206-214.
68. Rumble, J. R.; Lide, D. R.; Bruno, T. R., *CRC handbook of chemistry and physics*. Cleveland, Ohio, 1977; p 5-189.
69. Docherty, D.; Clydesdale, G.; Roberts, K. J.; Bennema, P., Application of Bravais-Friedel-Donnay-Harker, attachment energy and Ising models to predicting and understanding the morphology of molecular crystals. *Journal of Physics D: Applied Physics* **1991,** *24*, 89-99.
70. Donnay, J. D. H.; Harker, D., A new law of crystal morphology extending the Law of Bravais. *American Mineralogist* **1937,** *22*, 446-467.
71. Bach, S.; Panthöfer, M.; Bienert, R.; Buzanich, A. G.; Emmerling, F.; Tremel, W., Role of Water During Crystallization of Amorphous Cobalt Phosphate Nanoparticles. *Crystal Growth & Design* **2016,** *16* (8), 4232-4239.
72. De Yoreo, J., Crystal nucleation: more than one pathway. *Nat Mater* **2013,** *12* (4), 5-284.
73. De Yoreo, J. J.; Gilbert, P. U.; Sommerdijk, N. A.; Penn, R. L.; Whitelam, S.; Joester, D.; Zhang, H.; Rimer, J. D.; Navrotsky, A.; Banfield, J. F.; Wallace, A. F.; Michel, F. M.; Meldrum, F. C.; Colfen, H.; Dove, P. M., Crystallization by particle attachment in synthetic, biogenic, and geologic environments. *Science* **2015,** *349* (6247), aaa6760.
74. Rodriguez-Blanco, J. D.; Shaw, S.; Benning, L. G., The kinetics and mechanisms of amorphous calcium carbonate (ACC) crystallization to calcite, viavaterite. *Nanoscale* **2011,** *3* (1), 265-271.
75. Tobler, D. J.; Rodriguez-Blanco, J. D.; Dideriksen, K.; Bovet, N.; Sand, K. K.; Stipp, S. L. S., Citrate Effects on Amorphous Calcium Carbonate (ACC) Structure, Stability, and Crystallization. *Advanced Functional Materials* **2015,** *25* (20), 3081-3090.

Graphical Abstract:

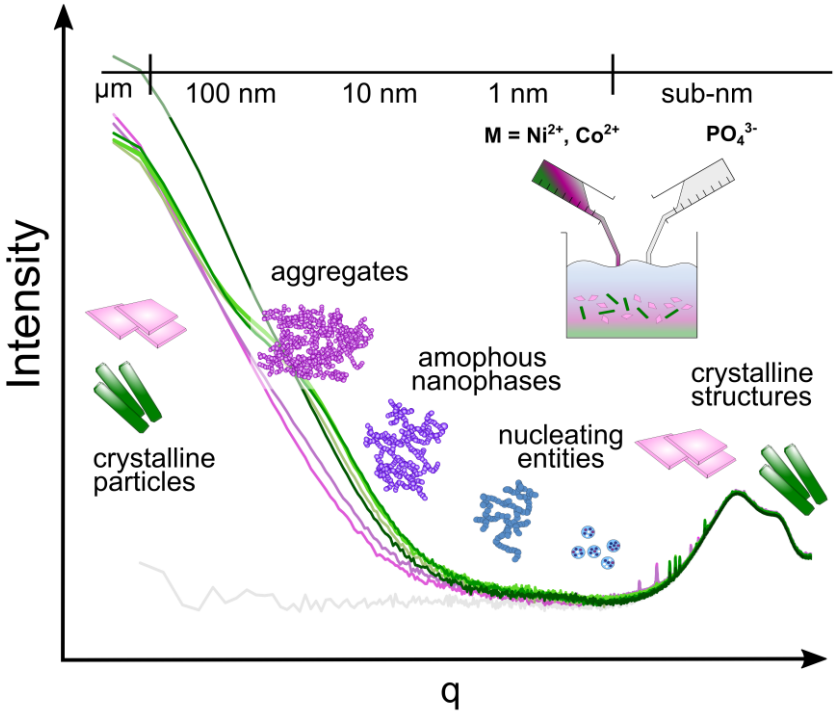

i